RSC Applied Interfaces

ROYAL SOCIETY OF CHEMISTRY

REVIEW

View Article Online
View Journal

Cite this: DOI: 10.1039/d6lf00009f

No substrate required: electron-beam-enabled, single-atom-thick 2D metals and metal oxides

Alicja Bachmatiuk,*[abc] Xiaoqin Yang,*[d] Maria Zdończyk,[a] Szymon Abrahamczyk,[a] Gražyna Simha Martynková[e] and Mark H. Rümmeli *[acfg]

Freestanding, single-atom-thick metals and metal oxides, defined here as monolayers suspended without an underlying solid substrate and supported only at their perimeter, represent an extreme two-dimensional (2D) limit that cannot be accessed by exfoliation of van der Waals solids. This review argues that their stability and formation are fundamentally interfacial: the most convincing realizations occur in edge-confined geometries (notably graphene pores) where perimeter anchoring, atom capture and boundary conditions stabilize low-coordination configurations that otherwise relax toward three-dimensional (3D) packing. In this context, a transmission electron microscope operates as an interface reactor, coupling atomic-resolution imaging to beam-driven diffusion, selective sputtering and reconstruction, such that fabrication and characterization are inseparable. We organize the literature into three experimentally relevant routes: (I) graphene-pore templating yielding membranes, planar patches and ultranarrow nanoribbons; (II) beam-driven top-down thinning and alloy-enabled dealloying concepts that bias reconstruction toward monoatomic remnants; and (III) subtractive beam chemistry converting compound precursors into new monolayers (*e.g.*, oxyhalide → oxide and $MoSe_2$ → Mo). We set out evidence and reporting standards (quantitative thickness assignment and dose-history reporting) and describe how automation and closed-loop control can translate these atomically thin interfaces from demonstrations to reproducible platforms.

Received 12th January 2026,
Accepted 4th May 2026

DOI: 10.1039/d6lf00009f

rsc.li/RSCApplInter

Introduction

Two dimensional (2D) materials can exhibit exceptional surface related properties because their atomic-scale thickness enhances surface sensitivity and induces quantum confinement. This has enabled phenomena such as the quantum Hall effect,[1,2] alongside very high electron mobility[3,4] and thermal conductivity,[5] and has driven intensive research over the last two decades. Many widely studied 2D materials, such as, graphene, *h*-BN, and transition-metal dichalcogenides (TMDs), share a common structural feature, namely, strong intralayer covalent bonding combined with weak interlayer van der Waals interactions. These weak interlayer forces allow straightforward exfoliation to obtain atomically thin layers. In contrast, elemental metals with largely isotropic metallic bonding typically favour 3D close-packed structures and are therefore not expected to exfoliate into stable 2D forms. As a result, most 2D materials research has historically focused on van der Waals solids.

Interest in 2D metals began to grow with reports of single-layer[6] and few-layer metallic structures.[7,8] Examples include potassium membranes on graphene, single-atom-thick Pb and In layers on Si(111),[9] Hf layers on Ir(111),[10] Rh nanosheets stabilized by poly-(vinylpyrrolidone),[11] and ultrathin Ga layers on various substrates.[12] In this context, the term 'metallene' has been introduced to describe metals that are non-layered in bulk yet can exist in a 2D layered form under suitable conditions.[12,13] By analogy, silicene denotes the 2D form of silicon,[14] while tin can form stanene[15,16] and germanium can form germanene.[17] Related elemental 2D materials such

[a] *Electron Beam Emergent Additive Manufacturing (EBEAM) Centre, Centre for Nanotechnology (CNT), Centre for Energy and Environmental Technologies (CEET), VSB-Technical University of Ostrava, 17. Listopadu 15, 708 33 Ostrava, Czech Republic. E-mail: mhr1967@yahoo.com*
[b] *Faculty of Chemistry, Wroclaw University of Science and Technology, Wybrzeze Wyspiarskiego 27, 50-370 Wroclaw, Poland*
[c] *Institute for Materials Chemistry, IFW Dresden, 20 Helmholtz Strasse, Dresden 01069, Germany*
[d] *Suzhou Laboratory, Suzhou 215123, China*
[e] *Nanotechnology Centre, CEETVŠB-Technical University of Ostrava, Ostrava 708 00, Czech Republic*
[f] *Soochow Institute for Energy and Materials Innovation, College of Energy, Key Laboratory of Advanced Carbon Materials and Wearable Energy Technologies of Jiangsu Province, Key Laboratory of Core Technology of High Specific Energy Battery and Key Materials for Petroleum and Chemical Industry, Soochow University, Suzhou 215006, China*
[g] *School of Smart Materials and Future Energy, Anhui Normal University, Wuhu 214002, China*

as antimonene[18] and plumbene have also been reported.[19] Although such systems are often discussed as potentially freestanding, by analogy with graphene, *h*-BN, and TMDs, robust experimental demonstrations of truly freestanding, single-atom-thick elemental metals remain scarce.

Note: in this review, we use the term freestanding in a deliberately strict sense: a metal (or metal oxide) sheet is considered freestanding only when the atomically thin region is suspended without an underlying solid substrate, such that both faces are exposed (typically to vacuum), and the structure is mechanically supported only at its perimeter (*e.g.*, suspended at the edge of a graphene pore perimeter or a nanoscale frame). We therefore distinguish freestanding membranes from (i) monolayers epitaxially bound to crystalline substrates (*e.g.* Pb and In on Si(111)[9,20] and Hf on Ir(111)[10,21]), (ii) films encapsulated or intercalated between 2D layers (*e.g.* Ag intercalated between SiC and graphene),[22] and Pd confined between graphene layers,[23] as well as multilayer alkali-metal structures)[24] (iii) ultrathin sheets resting on supports where substrate interactions can dominate structure and properties (*e.g.* Rh nanosheets stabilized by poly(vinylpyrrolidone)[11,25] and Ga layers on substrates[12,13]). This definition aligns the discussion with the central experimental challenge in the field: demonstrating the stability, structure, and properties of single-atom-thick metals and oxides in a genuinely substrate-free geometry.

A key milestone was the fabrication of a freestanding, single-atom-thick iron membrane by Rümmeli *et al.* in 2014 using an electron beam (e-beam) to drive the formation of the freestanding membrane.[26] This work provided direct evidence that 2D single-atom-thick elemental metals/metallenes can exist as a distinct class of 2D materials, and it highlighted electron irradiation as an enabling route to their formation. In that study, the transmission electron microscopes (TEM) imaging electron beam was used to mobilize surface atoms and small surface clusters at the graphene-vacuum interface of a monolayer graphene support, driving their reorganization into ordered Fe (crystalline) membranes suspended across graphene pores and thus using the pore edge as an interface-defined, edge-supported nanoreactor.

Motivated by this discovery, multiple theoretical studies predicted additional candidates for freestanding 2D elemental metals, including Au,[27] Ag,[28] and Cu.[29] Nevalaita *et al.*[30] carried out a systematic density functional theory (DFT) analysis of 45 metals, concluding that many candidate 2D metal structures are energetically more favourable in hexagonal or honeycomb geometries than in square lattices (Fig. 1).

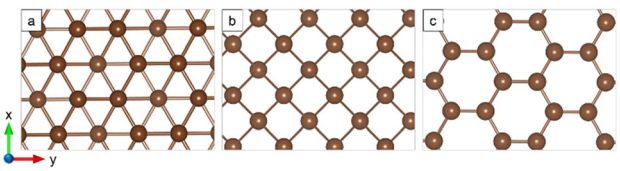

Fig. 1 Representative atomic structures of candidate two-dimensional metal lattices: (a) hexagonal (close-packed) lattice, (b) square lattice, and (c) honeycomb lattice.

Their analysis further emphasized that cohesive energy considerations are central: a stable 2D metal must balance sufficiently strong in-plane (2D) cohesion against comparatively weaker driving forces toward 3D bulk cohesion. If 2D cohesion is too low, the monolayer becomes unstable; if bulk cohesion dominates, 3D close-packed structures are preferred. Together, these theoretical insights and the early experimental demonstrations support the emergence of a new class of 2D elemental metals that can, under appropriate conditions, exist as freestanding structures. Later theoretical works moved beyond infinite, ideal sheets to address the finite-size and interface-controlled geometries that dominate experimentally. Nevalaita and Koskinen quantified edge and vacancy energetics across elemental 2D metals,[31] helping explain why finite patches are often favoured over extended monolayers. They further analysed the graphene-pore nanoreactor configuration using DFT combined with a liquid-drop description, showing how pore-edge stabilization and patch size govern which elements can persist as suspended 2D metals.[32] Because energetic minima may still be dynamically unstable, phonon-based calculations have also been used to assess dynamical stability across candidate 2D metal lattices.[33] In parallel, theory has proposed binary-alloy templates as a route to monatomic 2D metals *via* selective removal of a sacrificial component, providing design rules for top-down monolayer formation.[34]

Despite the growing theoretical landscape, experimentally verified freestanding single-atom-thick metals and oxides remain limited because their formation and survival seemingly require narrow processing windows. In practice, most reported structures are created and stabilized at (or near) the supporting specimen edge interface, where the electron beam simultaneously provides atomic-resolution metrology and delivers the energy/momentum needed for atom migration, bond rearrangement, and selective sputtering (knock-on). Consequently, the central question becomes not only which elemental systems can exist in a freestanding geometry, but also under what interfacial and irradiation conditions they can be reproducibly assembled, characterized, and maintained long enough for meaningful structure–property correlations.

In the remainder of this review, we organize the literature according to three experimentally relevant formation routes (Fig. 2): (I) graphene-pore templating, where graphene pores and their edges act as interface-defined nanoreactors that stabilize suspended membranes, ribbons, and planar clusters formed by beam-assisted assembly and/or reconstruction; (II) top-down thinning/dealloying, where selective removal from alloys or thicker metals yields monatomic metallic regions; and (III) subtractive beam chemistry, where suspended oxyhalides are converted into monolayer oxides by e-beam-driven dehalogenation.

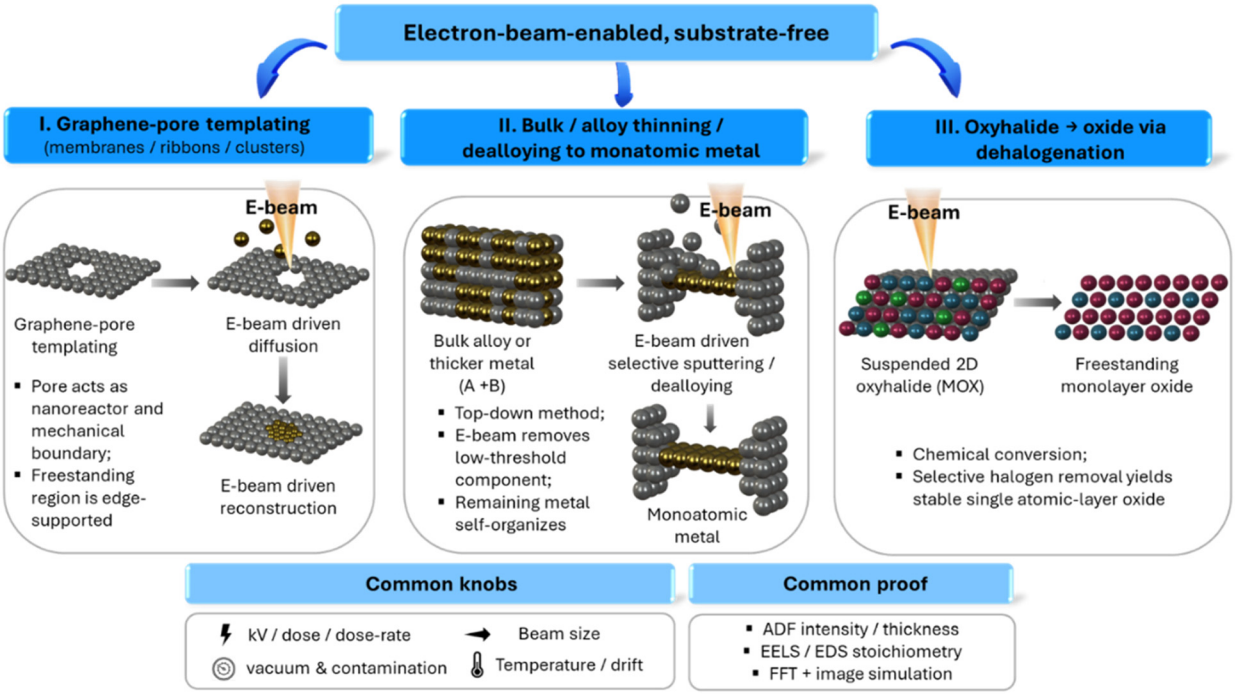

Fig. 2 Electron-beam-enabled, substrate-free routes to freestanding monoatomic metals and oxides. Schematic overview of three experimentally established formation pathways driven by electron irradiation: (I) graphene-pore templating, where pore edges localize atoms and stabilize suspended membranes, ribbons, or finite clusters; (II) top-down thinning or dealloying of bulk or alloy precursors, yielding self-limited monoatomic metal regions; and (III) subtractive beam chemistry, where suspended oxyhalides are converted into monolayer oxides *via* dehalogenation. Across all routes, the electron beam acts simultaneously as a metrology tool and an interface-confined process driver, with outcomes governed by dose, dose rate, scan strategy, and edge/interface geometry.

We then compare these routes using common criteria/evidence standards for single-atom thickness and freestanding character, dominant failure modes, and what is currently known (and not yet known) about intrinsic properties in a substrate-free geometry.

Electron beam–specimen interactions at interfaces (mechanisms and experimental control variables)

For truly freestanding, single-atom-thick metals and oxides, the electron microscope is not only an imaging platform but also an interfacial reactor: the beam couples the energy and the momentum directly into an atomically thin specimen whose two surfaces are exposed (typically to vacuum) and whose perimeter is defined by an interface (*e.g.*, a graphene pore edge). In this geometry, the beam can simultaneously enable formation, stabilize transient configurations, and drive degradation, so mechanistic clarity and careful reporting of irradiation conditions are essential.[35,36]

Electron irradiation (from the imaging electron beam) can affect a specimen through several pathways, commonly grouped as (i) elastic (knock-on) collisions, which can displace atoms and cause sputtering, and (ii) inelastic processes, including ionization/radiolysis, electronic excitations, electrostatic charging, and beam-induced heating;[37] in addition, hydrocarbon contamination and beam-stimulated surface diffusion can strongly bias outcomes at exposed interfaces.[35,36] In atomically thin systems, these processes are amplified because there is minimal bulk matter to dissipate energy and because edges, defects, and interfaces provide low-coordination sites where atomic rearrangement is facile.

In graphene-pore templating, typically, the decisive active region is the graphene-vacuum interface, particularly along the pore perimeter, where beam-stimulated migration and reconstruction can reorganize adatoms and clusters into suspended membranes. This behaviour is exemplified by the formation of freestanding Fe membranes within graphene pores under TEM irradiation.[26] For oxide-related routes, the beam can act either as a structural reorganizer or can trigger chemistry *via* bond scission and desorption. In graphene-pore systems, electron irradiation can promote the rearrangement of ZnO into a graphene-like (hexagonal) monolayer suspended in graphene pores, reflecting a beam-stimulated reconstruction process rather than exfoliation.[35] In oxide-native routes, electron irradiation can induce selective dehalogenation of suspended oxyhalides followed by lattice relaxation, yielding freestanding monolayer oxides (MOX → MO) under STEM conditions.[36] In alloy/thinning approaches, the same physical framework applies selective removal (by knock-on/sputtering) of a more weakly bound component can leave a reconstructed

monatomic metal region, again governed by local interface chemistry, defect density, and irradiation dose history.[37,38] Because the balance between formation and destruction is narrow for freestanding monolayers, the following parameters should be treated as primary experimental variables:

- Accelerating voltage (kV): sets the knock-on probability and strongly influences displacement/sputtering thresholds.[37,38]
- Total dose and dose rate: determine whether diffusion/reconstruction dominates (assembly) or whether net atom loss dominates (erosion); also affects contamination kinetics.[37]
- Beam mode and probe size (TEM *vs.* STEM): determine how localized the beam–specimen interaction is, *viz.*, broad, distributed illumination can promote more uniform diffusion/reconstruction across an area, whereas a tightly condensed STEM probe can drive highly localized thinning, sputtering, and edge reshaping at specific sites.[37,38]
- Environment and cleanliness: vacuum level, plasma cleaning, cryo/low-temperature options, and time-dependent contamination layers can stabilize or destabilize edges and interfaces.[37]
- Support/interface geometry: pore size/shape, edge termination, and availability of anchoring sites at the perimeter govern whether suspended structures persist long enough for robust characterization.[26]
- Time-resolved documentation: *in situ* sequences are often the most persuasive evidence linking irradiation conditions to a formation mechanism (assembly *vs.* conversion *vs.* thinning).[26,36]

Freestanding single-atom-thick 2D metal membranes in graphene pores

Graphene pores offer a rare experimental geometry in which elemental metals can meet our strict freestanding definition: an atomically thin metal region spans an opening without an underlying solid substrate, while mechanical stability is provided only through perimeter anchoring at the graphene edge interface. In this setting, the pore perimeter acts as an interface-defined boundary condition that (i) localizes mobile atoms, (ii) constrains out-of-plane relaxation, and (iii) stabilizes low-coordination metal configurations that would otherwise undergo out-of-plane densification and 3D aggregation into close-packed clusters. Consequently, monoatomic metal membranes in graphene pores should be viewed as interface-stabilized, beam-assisted assembled phases, not as exfoliated analogues of van der Waals monolayers.[26,37,38]

Interface-controlled assembly under the electron beam

The formation pathway is typically a coupled sequence: (1) a local atom reservoir (adatoms, nanoparticles, or decomposed precursors) is present on/near graphene; (2) electron irradiation activates surface diffusion and interface mass transport; (3) atoms are trapped at the pore perimeter where bonding to edge sites and geometric confinement lower the effective penalty for 2D coordination; and (4) lateral ordering/reconstruction produces a suspended monolayer spanning the pore. In this regime, the beam has a dual character, namely, that of simultaneous metrology (atomic-resolution imaging and spectroscopy) and that of process driver (diffusion, bond rearrangement, and element-selective atom loss). In particular, when the atom reservoir is a compound (*e.g.*, an oxide) or an alloy, electron irradiation can drive selective atom removal (preferential sputtering and/or beam-stimulated desorption), shifting the local composition toward the more irradiation-resilient component and enabling an interfacial transformation (*e.g.*, CrO → Cr) followed by reconstruction into a monolayer at the pore edge.[37–39] This explains why reproducible formation requires a narrow operating window in voltage/dose/dose-rate and edge condition.[37,38] A useful way to rationalize why pores can stabilize membranes is through the competition between (i) in-plane cohesion of the 2D metal lattice, (ii) edge energies of finite patches, and (iii) stabilization at the graphene–metal interface. This finite-size plus interface perspective, formalized in later theory work (edge/vacancy energetics; liquid-drop style scaling in pores), helps explain why experiments often yield finite islets or evolve toward ribbons, even when extended membranes are transiently accessible.[31,32]

Fe and Cr as archetypes of pore-spanning 2D metal membranes

The first widely recognized experimental proof is the *in situ* formation of crystalline, single-atom-thick Fe membranes suspended in graphene pores.[26] An alternative theoretical interpretation suggests that the observed structures may correspond to two-dimensional iron carbide phases stabilized in graphene pores.[40] However, electron energy loss spectroscopy (EELS) in the original study did not indicate carbon within the membrane region, supporting the assignment to metallic Fe.[26] As shown in Fig. 3(a–e), mobile Fe atoms/clusters at the graphene-vacuum interface reorganize into an ordered pore-spanning lattice. Beyond the visual impact, the study established a new standard evidentiary logic for single-atom-thick freestanding membranes, namely: atomic-resolution imaging of a periodic lattice, reciprocal-space/FFT analysis, and quantitative comparison of normalized intensity profiles between experimental micrographs and image simulations to confirm a monolayer rather than a multilayer stack.[26] A key extension is the single-atom-thick Cr membrane, also formed in graphene pores and supported by image simulations and DFT (including an antiferromagnetic ground state), illustrating that pore-templated membranes can serve as platforms for intrinsic 2D metallic and, potentially spin-related physics, at the atomic limit.[39] In Fig. 3(f–h), the Cr example also highlights how spectroscopy and simulation

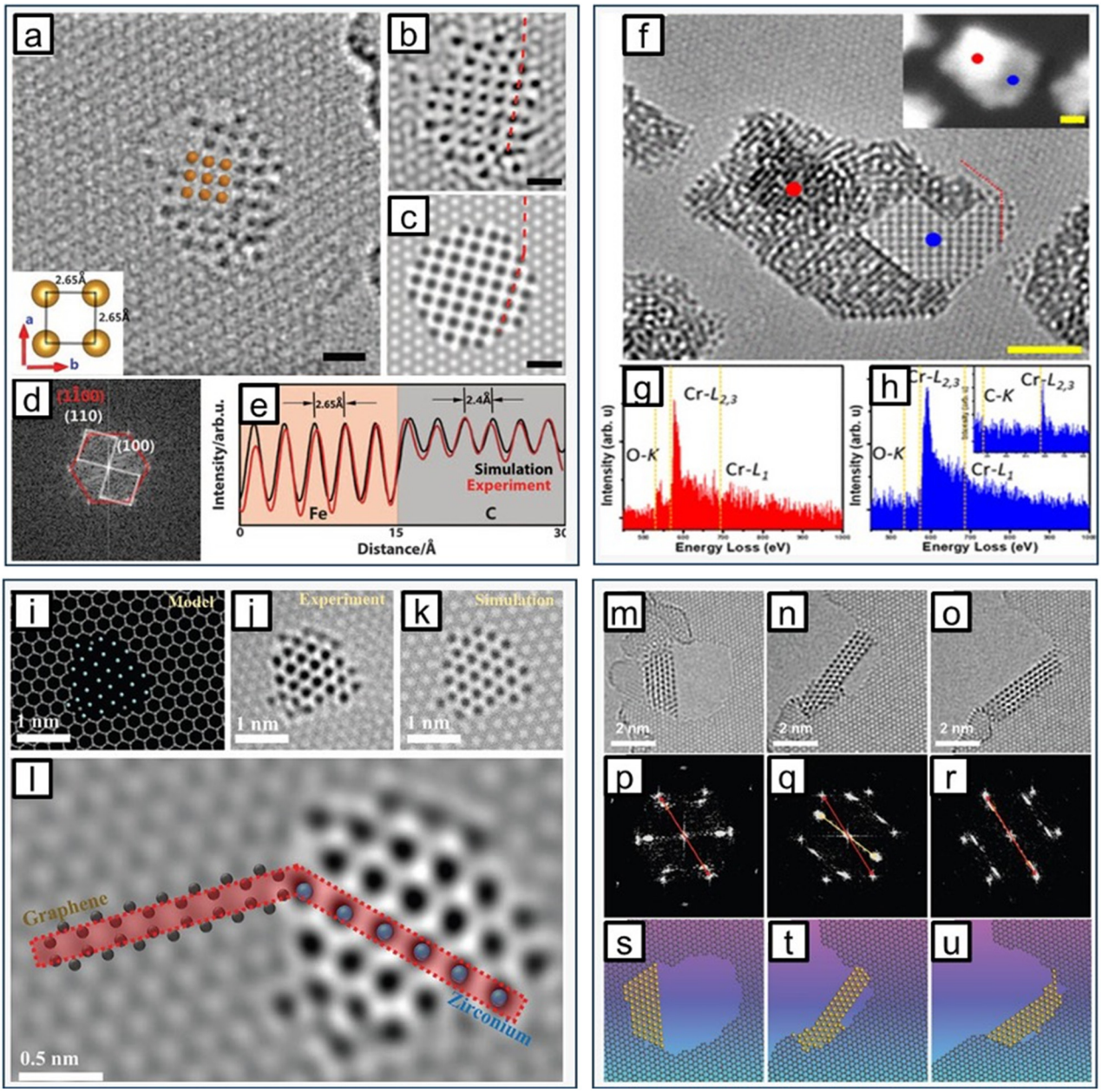

Fig. 3 Lattice investigation of different membranes suspended in graphene pores. (a) LVACTEM micrograph of a monoatomic Fe layer with the square unit cell. The inset highlights the interatomic spacing of the square unit cell. (b) Smoothed image of (a). (c) Image simulation of a monoatomic Fe layer. (d) Fast Fourier transform of the structure in (a) that shows the lattice relationship between the graphene (red) and the monoatomic Fe layer (white). (e) Normalized intensity profiles from the image simulation (black line) and experimental image (red line), corresponding to marked profiles in red dashed lines in (b) and (c). The intensity profiles match, confirming that the Fe membrane is a single atom thick. All scale bars, 0.6 nm. Reproduced with permission.[26] Copyright 2014, American Association for the Advancement of Science. (f) HRTEM micrograph of the CrO NP, Cr membrane with square lattice and graphene suspension support. The inset STEM image corresponds to the HRTEM image and highlights the positions where local EELS was acquired. (g and h) Local EELS spectra of CrO NP (red spectrum) and 2D Cr membrane (blue spectrum) measured from red and blue dots in (f), respectively. Reproduced with permission.[39] Copyright 2020, American Chemical Society. (i) Top view model of the 2D Zr inside a graphene pore. (j) Experimental TEM image of a typical zirconene islet and (k) TEM simulation of the zirconene inside the graphene pore. (l) Regions from where the intensity line profiles of the Zr and C atoms. Reproduced with permission.[41] Copyright 2025, Wiley-VCH. (m) Single-atom-thick Au crystal suspended in a graphene hole; (n) suspended two-dimensional (2D) single-atom-thick Au nanoribbon; (o) Au nanoribbon attaching to the graphene edge; (p–r) the fast Fourier transform of the structures corresponding to (m–o) show lattice relationship between graphene (red arrow) and Au nanostructures (yellow arrow); (s–u) the stick and ball model (m–o), respectively. Reproduced with permission.[42] Copyright 2020, Wiley-VCH.

are commonly used in combination to underpin elemental assignment and monolayer thickness. Mechanistically, Cr further emphasizes that pore-templated membranes can couple geometrical stabilization to beam-enabled interfacial

chemistry (*e.g.*, formation/reduction steps at the pore edge), reinforcing the need to interpret these membranes as outcomes of a coupled beam–interface system rather than as purely thermodynamic equilibrium structures.[37–39] The pore-templated family has recently expanded beyond these early transition-metal exemplars. Fig. 3(i–l) show suspended zirconene islets grown inside graphene pores, demonstrating that interface-defined assembly in pores can yield stable monoatomic 2D domains for additional metals and reinforcing that the graphene pore acts as a general nanoreactor in which atom supply, edge anchoring, and irradiation history (*i.e.*, time-dependent beam conditions: voltage, dose, dose rate, and scan/dwell protocol) jointly determine the accessible 2D metal outcome.[41] Dedicated experimental reports of pore-spanning Au monolayers in graphene pores are comparatively limited, but a key *in situ* TEM study reports single-atom-thick Au membranes and nanoribbons suspended in graphene pores, and captures dynamic membrane-to-ribbon evolution as pore geometry and boundary conditions change under irradiation (Fig. 3m–u).[42] This emphasizes that Au atomic configurations in pores are not a fixed phase but an interfacial state: atom supply, pore evolution, and edge anchoring can bias the outcome toward compact pore-filling membranes or toward elongated ribbons.[42]

Theory provides unusually direct support for Au-in-pore formation pathways. DFT modelling indicates that Au is weakly bound on basal graphene but preferentially trapped at graphene edges, and that atom transport from graphene toward the pore perimeter can proceed along low-barrier pathways, making pore-edge capture and lateral growth plausible under experimental conditions.[43] Complementarily, quantum molecular dynamics simulations predict that nanoscale Au patches suspended in graphene pores can access an atomically thin 2D liquid phase, highlighting extreme fluxionality as a realistic state for nanoscale Au under confinement and irradiation.[44] Together, these results suggest that Au in graphene pores should be discussed in terms of a size, edge, and irradiation-dependent phase space spanning ordered membranes, ribbons, and highly mobile (liquid-like) 2D patches.[41,43,44]

Freestanding oxide membranes in graphene pores: reconstruction, stoichiometry, and interfacial stabilization

Freestanding oxide membranes in graphene pores occupy a distinct niche relative to elemental metal membranes: they are stabilized by the same perimeter anchoring at the graphene pore edge, but their formation and survival are additionally shaped by bond polarity, stoichiometry control, and irradiation-driven reconstruction. Because oxides often have multiple competing coordination environments (and frequently do not possess a naturally layered bulk analogue), graphene pores provide an interface-defined geometry in which electron irradiation can steer the system toward atomically thin suspended phases that are difficult to access by conventional growth or exfoliation.

An example is graphene-like monolayer ZnO (g-ZnO) in pores (Fig. 4a–j). *In situ* TEM studies show that Wurzite ZnO can reorganize inside graphene pores into a graphene-like (hexagonal/honeycomb) ZnO monolayer (and in some cases bilayers) suspended across the pore opening.[35] The key

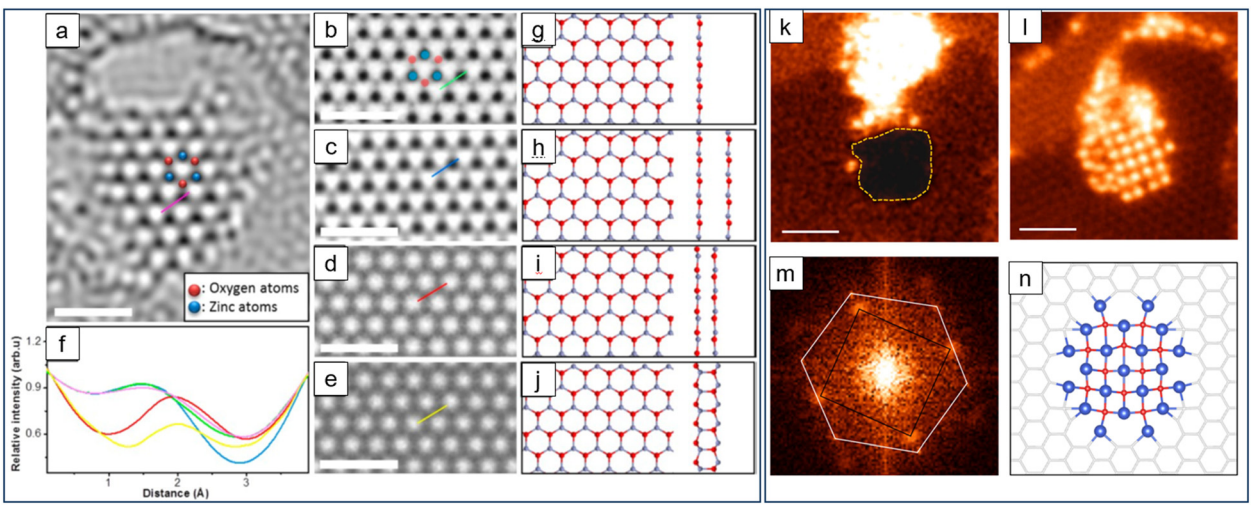

Fig. 4 Characterization of free-standing membranes suspended in a graphene pore. (a) TEM image of g-ZnO membrane in graphene hole. (b–e) Image simulation of single-layer and bilayer T1, T2, and wurtzite structure of ZnO, respectively. (f) Normalized intensity profiles from the TEM image (pink line) and from the simulated image of single-layer (green line), bilayer T1 (blue line), bilayer T2 (red line), and bilayer wurtzite (yellow line), corresponding to marked profiles in pink, green, blue, red, and yellow line in (a–e). (g–j) Stick and ball models of ZnO corresponding to images in (b–e). All scale bars = 1 nm. Reproduced with permission.[35] Copyright 2015, American Chemical Society. (k) A Cu oxide cluster at the edge of a graphene pore (highlighted). (l) A CuO monolayer suspended in a graphene pore. (m) FFT of (l), which shows the lattice relationship between graphene and copper oxide monolayer. (n) A theoretical model of a CuO membrane suspended in a graphene pore. Scale bars: 1 nm. Reproduced with permission.[45] Copyright 2017, IOP Publishing.

scientific point is that this is a reconstruction pathway, not exfoliation: bulk ZnO is wurtzite, whereas the suspended membrane adopts a planar honeycomb network that is compatible with pore-edge boundary conditions. The panels in Fig. 4(a–j) capture the core evidence chain used for such assignments, *viz.*, atomic-resolution images with lattice periodicity in the suspended region, structural overlays identifying Zn/O sublattices, and quantitative intensity-profile comparisons supporting single-layer character.[35] From a broader materials perspective, g-ZnO has also been discussed as a stabilized 2D oxide polymorph with distinctive bonding and properties compared with bulk ZnO, reinforcing why these pore-stabilized membranes are scientifically meaningful beyond microscopy.[46] A complementary oxide case is the formation of single-atom-thick copper oxide (CuO) monolayers, reported as freestanding sheets formed in graphene pores, and also observed on graphene supports – Fig. 4(k–n).[45] This example is valuable because it demonstrates that pore stabilization is not restricted to honeycomb reconstructions: CuO monolayers can adopt a square-lattice motif at the atomic limit, underscoring that graphene pores can stabilize non-van der Waals 2D oxide lattices when the irradiation regime and edge anchoring conditions favour ordering over sputtering.[45]

Finite planar clusters and sub-nanometre patches in graphene pores

While pore-spanning (membrane diameter) Fe/Cr (and, in selected cases, Au and Zr) indicate a membrane size limit, a large fraction of experimentally accessible freestanding 2D metals appear first as finite, atom-countable patches, *i.e.*, intermediates between isolated adatoms and extended membranes. Fig. 5 captures this regime and supports a key point for the graphene-pore route: pores do not only template continuous sheets; they also stabilize discrete, single-atom-thick 2D islands whose structure is governed by finite-size energetics and pore-edge interactions. Dong *et al.* tracked the evolution of small Pt clusters on suspended graphene under electron irradiation and showed that clusters can become trapped at hole edges, evolve together with hole enlargement, and progressively flatten/reshape as the local graphene boundary condition changes (Fig. 5(a–f)).[47] In the context of freestanding, this is a useful boundary case: the metal does not span the pore as a membrane, but the mechanically decisive interface is still the pore perimeter, which pins the cluster and can bias the structure toward planar motifs once edge bonding becomes dominant.[47] This example highlights a coupled pathway, namely, electron beam driven migration and restructuring of the metal occurs alongside irradiation-driven evolution of the graphene boundary, rather than metal rearrangement in isolation.[37,47] A complementary illustration is provided by the single-atom-thick Sn patches reported by Yang *et al.*, where planar Sn clusters/patches (approximately 1–8 atoms) are stabilized inside graphene pores and show a clear size-dependent structural progression from discrete motifs toward more extended, ordered 2D configurations (Fig. 5(g and h)).[48] Here, DFT calculations indicate that edge interactions are not a minor perturbation: cluster geometries expected for free (edge-unconstrained) Sn increasingly deviate from experiment as size increases, consistent with the pore perimeter providing stabilizing interactions and shifting the relative stability of competing 2D motifs.[48] This behaviour is consistent with broader theoretical analyses showing that edge and vacancy energetics can dominate stability rankings across elemental 2D metals, such that finite patches can be favoured over extended monolayers under experimentally accessible conditions.[31,32]

These planar-cluster observations also emphasize that the relevant active zone is the evolving graphene edge interface: adatoms and small clusters migrate on graphene and can be preferentially trapped at undercoordinated sites associated with pore edges and vacancies,[49,50] while continued

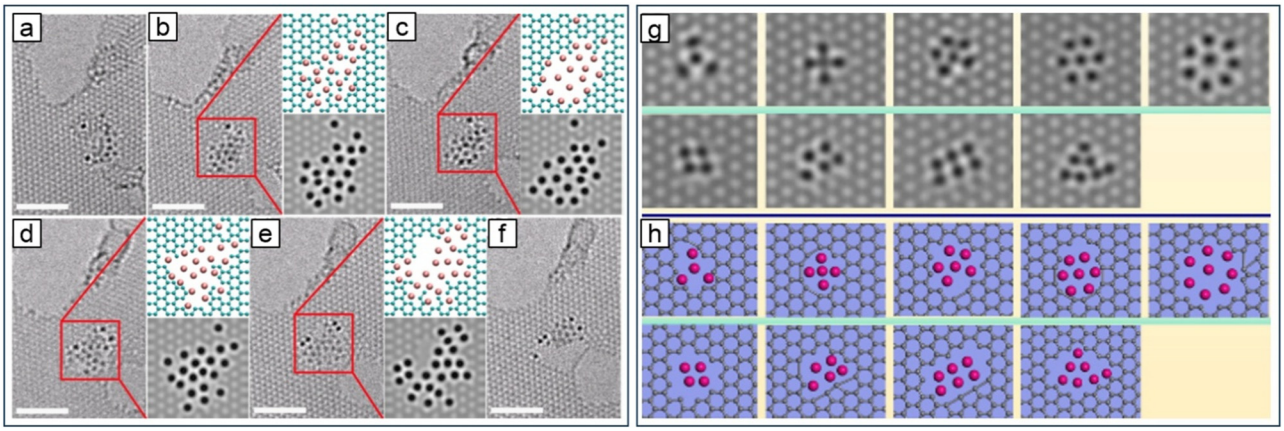

Fig. 5 Pt and Sn clusters embedded in a graphene pore. (a–f) Image sequence shows the evolution a Pt-graphene composite. The insets in panels (b), (c), (e), and (f) show atomic models corresponding to the regions highlighted by red squares. Scale bar: 2 nm. Reproduced with permission.[47] Copyright 2013, ASME. Image simulations (g) and top-view stick-and-ball models (h) for different forms of in-plane single-atom thick 2D Sn patches. Reproduced with permission.[48] Copyright 2020, Springer Nature and Tsinghua University Press.

irradiation reshapes the pore boundary (defect creation and hole growth), continuously changing the interfacial constraints that select the observed metal configuration.[37,47] As a result, time-resolved *in situ* sequences, coupled with atomic-resolution imaging and modelling, are often the most persuasive evidence that a given motif is a genuinely single-layer planar patch rather than a projected 3D cluster.[47,48]

Beam-assembled ultranarrow nanoribbons in graphene pores

While pore-spanning monoatomic membranes (as discussed in the preceding sections) represent the most visually direct realization of freestanding 2D metals/oxides, Fig. 5g emphasizes a second, equally important outcome of graphene-pore confinement under irradiation: ultranarrow, single-atom-thick metal nanoribbons that evolve from (or in competition with) small 2D patches. In this regime, the system is still governed by the same core ingredients, *viz.*, an atom reservoir, beam-activated surface/interface transport, and strong trapping/anchoring at undercoordinated graphene edge sites, however, the morphological selection shifts toward high-aspect-ratio 1D growth rather than compact 2D pore filling. This is consistent with the finite-size/interface picture developed for elemental 2D metals, where edge energies and pore-edge stabilization can dominate over bulk-like 2D cohesion, causing experimentally observed structures to preferentially persist as finite patches or anisotropic motifs instead of extended sheets.[31,32] In practice, irradiation simultaneously reshapes the graphene boundary (defect creation and hole evolution) and drives atom migration/reconstruction, so the ribbon outcome should be viewed as a kinetically selected interfacial state within a narrow dose/dose-rate/voltage window rather than a simple equilibrium phase.[37,38]

In Fig. 6(a–d), time-resolved imaging shows that continued electron irradiation drives a progressive thinning and reconstruction pathway in which a Mo-containing 2D precursor loses material (*via* knock-on/sputtering and associated rearrangements) while the remaining atoms are redistributed and stabilized by pore-edge trapping, culminating in a highly localized, ultranarrow nanoribbon, consistent with a subtractive (top-down) formation route where preferential atom removal and beam-activated mass transport concentrate the more irradiation-resilient component into an effectively monatomic-thickness filament.[37,38,51] Conceptually, the beam provides (i) momentum transfer that can preferentially remove the more weakly bound/lower-threshold species, and (ii) sustained activation of surface diffusion, enabling the surviving species to be captured and reorganized at the evolving graphene interface.[37,38] The important mechanistic point is that the ribbon does not merely "appear" as a carved remnant: it emerges through continuous mass transport to, and along, the graphene edge, where trapping and coordination to the pore perimeter can stabilize an atomically thin configuration against 3D thickening.[31,32,37]

In the zirconium example (Fig. 6(e–j)), the initially compact Zr-containing patch does not remain as a stable islet; instead, sustained irradiation drives edge-mediated reshaping and material loss such that the patch elongates and reorganizes into an ultranarrow Zr-based nanoribbon, again emphasizing nanoribbon formation as the preferred long-lived endpoint under these beam/interface boundary conditions.[37,38,41] Here, pore-edge anchoring provides the boundary condition that both stabilizes the monatomic thickness and biases growth/

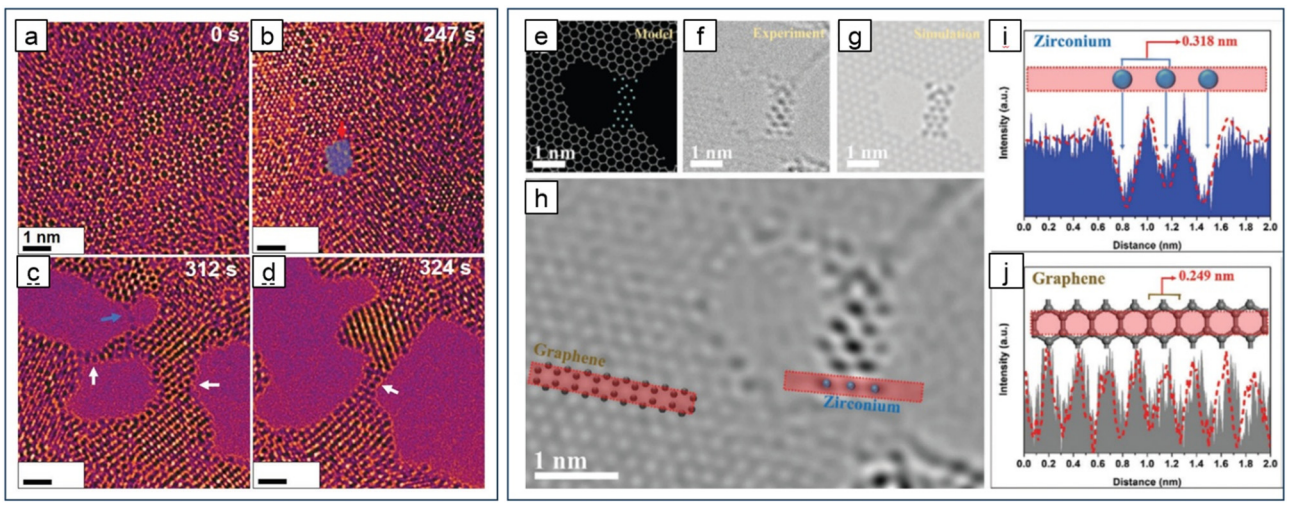

Fig. 6 High-magnification microscopy images showing the formation of a Mo nanoribbon through extended electron irradiation of a $Mo_2Ti_2C_3$ monolayer and subsequent Mo nanoribbon formation at (a) O s, (b) 247 s, (c) 312 s, and (d) 324 s. White arrows indicate Mo nanoribbons. Red arrow indicates an N-doped graphene membrane. Reproduced with permission.[51] Copyright 2020, Wiley-VCH. Formation of zirconium nanoribbon. (e) Top view model of the Zr nanoribbon attached to opposing graphene edges. (f) Experimental TEM image of a typical Zr nanoribbon and (g) TEM simulation of the Zr nanoribbon inside the graphene pore. (h) Regions from where the line profiles of the (i) Zr nanoribbon and (j) graphene were extracted. Reproduced with permission.[41] Copyright 2025, Wiley-VCH.

reshaping along a preferred direction, while the electron beam maintains a flux of mobile atoms and continuously modifies the local interface (edge structure, termination, and available binding sites).[37,38,41] The resulting ribbon geometry underscores that, in graphene pores, 2D metals can manifest experimentally as atomically thin domains with strong anisotropy, membranes, patches, or ribbons, depending on atom supply, edge chemistry, and the irradiation history.[31,32,41] More broadly, these Zr and Mo examples reinforce an evidence standard that becomes especially important for ultranarrow objects: time-resolved sequences plus atomic-resolution contrast analysis/simulation are often essential to distinguish a genuinely single-atom-thick ribbon/patch from a projected 3D cluster evolving in thickness.[37,38]

Top-down thinning and alloy-enabled routes to monatomic sheets

Fig. 7 highlights a complementary top-down logic for accessing freestanding monoatomic metals: rather than assembling a full pore-spanning membrane directly, the electron beam can drive thickness self-limitation and/or selective atom removal from thicker precursors (including alloys), with reconstruction occurring under the combined influence of irradiation, surface diffusion, and edge/interface stabilization.[37,38] On the experimental side, Wang *et al.* reported free-standing monatomic-thick two-dimensional gold and established a rigorous thickness-verification workflow using quantitative atomic-resolution annular dark-field scanning transmission electron microscopy (ADF-STEM) contrast analysis (Fig. 7(a–f)).[52,53] The key point is not only that Au can exist transiently as a single-atom-thick sheet in a substrate-free geometry, but that the monolayer assignment is supported quantitatively. Namely, line profiles across adjoining regions distinguish monolayer-like and bulk-like contrast, intensity histograms separate discrete thickness populations, and atom-counting maps reveal an extended interior dominated by single-atom columns (with thicker regions typically localized near boundaries), consistent with a self-limited monoatomic configuration rather than a projected thin wedge of 3D material.[52,53] Fig. 7 also illustrates why binary alloys are attractive precursors for monatomic 2D metals: selective sputtering can, in principle, remove one component while leaving the other behind to reconstruct into a stable atomically thin remnant, provided there is a sufficiently large separation in knock-on stability and a realistic kinetic pathway for edge-trapped reorganization.[37,38] Nevalaita and Koskinen formalized this concept by proposing free-standing 2D metals from binary metal alloys and mapping alloy pairs in terms of selective-removal feasibility (Fig. 7g).[34]

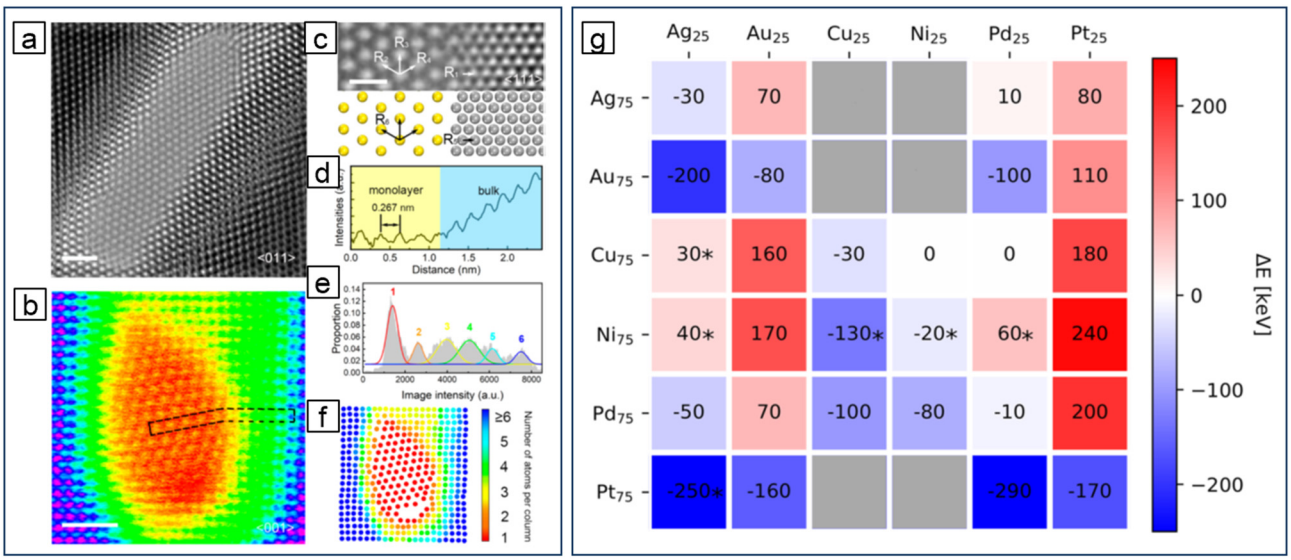

Fig. 7 Electron micrographs and structure of fabricated monolayer Au membranes and alloy formation energies for 30 binary combinations. (a) AC-HRTEM image of a typical monolayer Au membrane with closely packed hexa-coordinate lattice framed in bulk Au–Ag alloy along <011> zone axis. (b) HAADF-STEM image of a monolayer Au membrane framed in bulk Au–Ag along <001> zone axis. (c) AC-HRTEM image of monolayer Au membrane and bulk Au–Ag alloy viewing along <111> zone axis. Corresponding atomic structures are illustrated in the lower panel. R1, R2, R3 and R4 are experimentally measured (projected) atomic distances. R5 and R6 are theoretical (projected) atomic distances. (d) Line profile of HAADF-STEM image intensity revealing monolayer (yellow shadowed) and bulk (blue shadowed) regions along the black dashed box in (b). In-plane Au–Au distance in the monolayer Au membrane is indicated by the black arrow. (e) Histogram of HAADF-STEM image intensities of atom columns. The peaks are shown as differently coloured Gaussian curves fitting from the histogram. (f) The mapping of number of atoms per atom column along the direction of observation. The atom positions and intensities are measured from (b). Scale bars, 1 nm in (a) and (d), 0.5 nm in (c). Reproduced with permission.[40] Copyright 2019, American Chemical Society. (g) Alloy formation energies for 30 binary combinations. Positive energy (red colour) indicates the exothermic alloy formation. Reproduced with permission.[34] Copyright 2020, American Institute of Physics.

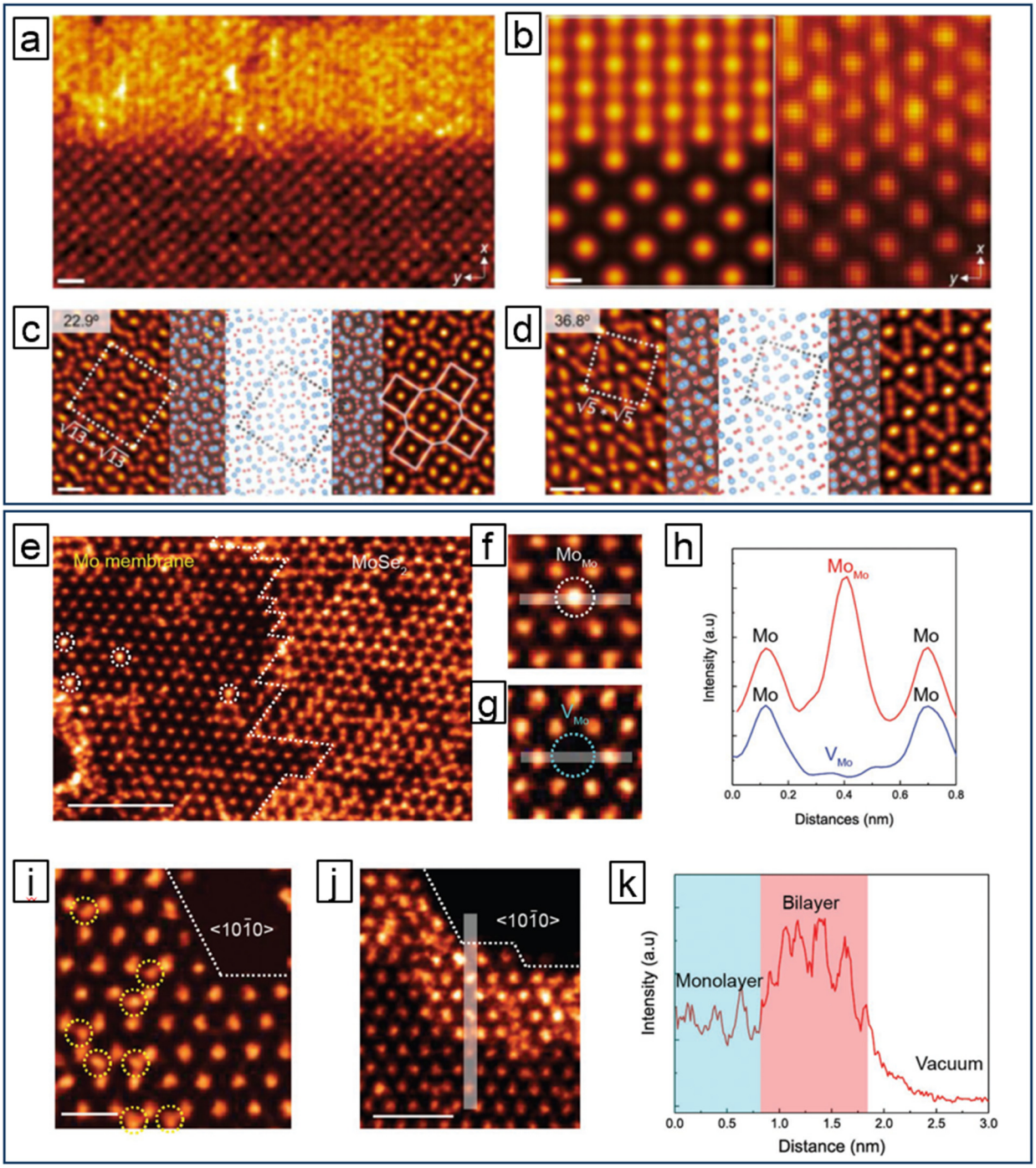

Fig. 8 Fabrication of coherent CrOCl–CrO heterostructures and twisted CrO bilayers. (a) Low-magnification STEM-ADF image of a CrOCl–CrO interface. Scale bar: 0.5 nm. (b) Atomic-resolution STEM-ADF image (right) of a CrOCl–CrO interface with the corresponding simulated image (left) overlaid. Scale bar: 0.2 nm. (c) and (d) Atomic-resolution STEM-ADF images (left), the corresponding structural models (middle), and simulated images (right) of the 22.9° (c) and 36.8° (d) twisted CrO bilayers. Reproduced with permission.[36] Copyright 2025, Springer. Structural properties of the as-fabricated monolayer Mo membrane. (e) STEM-ADF image showing phase boundaries (highlighted by the white dashed lines) between the as-fabricated monolayer Mo membrane and parental monolayer $MoSe_2$ film. (f) and (g) STEM-ADF images of a MoMo site (b) and a VMo vacancy site in the monolayer Mo membrane (g). (h) Intensity line profiles showing the MoMo (red line) and the VMo (blue line). (i) STEM-ADF image depicting exposed atomically sharp edges along the ⟨10 10⟩ directions as highlighted by the white dashed lines in the monolayer Mo membrane. Remaining Se atoms are highlighted by yellow dashed circles. (j) STEM-ADF image of a bilayer Mo membrane, which takes AA stacking registry. (k) Intensity line profile revealing the monolayer (cyan) and bilayer (red) regions in (j). Scale bars: 2 nm in (a), 0.5 nm in (e), and 1 nm in (f). Reproduced with permission.[55] Copyright 2018, Wiley-VCH.

Their calculated ΔE matrix (a computed selectivity metric describing how strongly one alloy component is expected to be removed relative to the other) provides a practical design rule: alloy combinations that create a substantial irradiation selectivity window are the most promising candidates for beam-driven dealloying into monatomic 2D sheets, whereas pairs with limited selectivity are less likely to yield clean monoatomic products before the remaining species is also destabilized.[34] In the context of graphene-pore and edge-confined geometries, this alloy-enabled route connects naturally to the broader interface picture developed for pore systems, *viz.*, finite-size energetics and edge stabilization can dominate morphology. Hence, the experimentally accessible outcomes may include monatomic sheets, ultrathin patches, or narrow filaments depending on atom supply, boundary evolution, and dose history.[31,32,34,37,38]

Subtractive electron beam chemistry: monatomic metal oxides and metals from compound precursors

Fig. 8 introduces a distinct formation route in which the electron beam does not merely rearrange atoms at an interface, but drives selective chemical subtraction (removal of an anion/ligand sublattice) in suspended precursors, followed by rapid lattice relaxation into new atomically thin phases under edge/interface constraints.[37,38,54] In this class of experiments, the key reactor variables are the same beam control variables (voltage, dose rate, probe dwell history) emphasized earlier, but the decisive outcome is conversion: a parent compound is transformed into a new 2D phase by preferential sputtering/desorption and beam-stimulated diffusion, with the perimeter/edge providing the stabilization needed for a single-atom-thick product to persist long enough for atomic-resolution validation.[37,38] In the oxyhalide-derived route (Fig. 8, top), time-resolved STEM reveals beam-driven dehalogenation of suspended layered metal oxyhalides (MOX) followed by lattice relaxation into freestanding single-atomic-layer metal oxides (MO).[36] The time-resolved STEM data illustrates beam-driven dehalogenation of suspended layered metal oxyhalides, producing freestanding, single-atomic-layer metal oxides that are structurally well-defined rather than amorphous remnants.[36] A central message is that this route expands the accessible freestanding library beyond elemental metals: monolayer oxides can be stabilized in substrate-free geometries with lattice motifs that are not constrained to honeycomb networks (*e.g.*, square-like oxide lattices), and the resulting layers can form twisted bilayers and moiré superlattices when rotationally misaligned domains overlap, providing an immediate structural handle for tuning emergent electronic/magnetic behaviour at the atomic limit.[36]

Mechanistically, Fig. 8(a–d) highlights that the product is selected by (i) removal of halogen species under irradiation and (ii) reconstruction into a lower-dimensional oxide lattice whose stability is enhanced by confinement and edge anchoring, rather than by exfoliation from a naturally layered oxide bulk.[36–38]

The lower panels (Fig. 8(e–k) show an analogous subtractive conversion in a different precursor family, where Zhao *et al.* used electron irradiation to transform a $MoSe_2$ chalcogenide into a freestanding monolayer molybdenum membrane, with atomic-resolution ADF-STEM providing clear monolayer-bilayer thickness discrimination and revealing point-defect motifs (*e.g.*, Mo vacancies) within the membrane.[55] Here, preferential loss of the chalcogen sublattice under irradiation is a chemically meaningful step (not just damage), because it can drive local stoichiometry toward a metal-rich state while the edge/interface region stabilizes an atomically thin Mo configuration against immediate thickening.[55,56] The broader implication is that layered chalcogenides (and related compounds) can serve as built-in reservoirs/templates for freestanding monatomic metals: the beam both supplies the subtraction chemistry (selective sputtering/desorption) and provides the mobility needed for reconstruction, so that "single-atom-thick metal" can be reached from a 2D parent compound without requiring direct deposition/assembly of a pore-spanning metal sheet from external adatoms.[37,38,55,56] Taken together, the studies define a practical, experimentally grounded category: beam-enabled subtractive chemistry converts suspended precursors into new freestanding monolayers (oxides or metals), and the most convincing demonstrations rely on (i) atomic-resolution imaging with quantitative contrast/line-profile support for single-layer assignment and (ii) time-sequenced evidence linking irradiation history to conversion and reconstruction pathways.[36–38,54,55]

Future outlook and opportunities for automation, ML, and AI

Looking ahead, the field's central challenge is shifting from demonstrating the existence of freestanding monoatomic metals/oxides to making them reproducible, comparable across laboratories, and application relevant. Because these systems occupy a narrow stability window set by displacement thresholds, inelastic processes, contamination kinetics, and edge/interface energetics,[37,38] progress will increasingly depend on controlling and reporting irradiation conditions with the rigor typically reserved for synthesis and processing in conventional materials growth. For monoatomic products fabricated from 2D precursors (*e.g.*, $MoSe_2$), this requirement becomes even more explicit: radiation damage pathways and defect evolution must be treated as part of the process recipe, because fabrication and characterization are inseparable in electron-beam-enabled routes.[35–38,54,56] More generally, damage in TEM/STEM is often a coupled competition among knock-on, radiolysis/ionization, charging, and local chemistry, and it can be strongly material- and

environment-dependent, particularly for insulating/ionic compounds and oxides.[57,58] A near-term priority is therefore an evidence and metadata standard that is integral to every claim of freestanding monoatomic thickness: (i) quantified thickness assignment (preferably using quantitative/standardless STEM workflows with uncertainty estimates),[53] (ii) explicit dose history and dose-rate reporting (not only accelerating voltage),[37] (iii) time-resolved sequences that connect irradiation conditions to mechanism and outcome (assembly *vs.* conversion *vs.* thinning),[26,36,55] and (iv) description of edge geometry/support evolution and cleanliness state (since the perimeter is both a mechanical boundary condition and a chemically active interface).[37,38] This level of rigor is particularly important for ultranarrow ribbons and finite patches, where projection effects and boundary thickening can otherwise mimic monolayer character.[31,32,37,38] In this context, long-standing insights from irradiation-driven microstructural evolution—particularly the dominant role of edges and undercoordinated sites—remain highly relevant at the 2D limit, as further supported by recent *in situ* TEM/STEM studies of beam-induced defect formation and structural transformations in low-dimensional materials.[54,59–62]

On the fabrication side, two routes appear especially scalable once paired with better control software: subtractive conversion (precursor → monoatomic membrane) and top-down thinning/dealloying. Subtractive conversion is exemplified by atom-by-atom fabrication of monolayer Mo membranes from $MoSe_2$, where atomic-resolution ADF-STEM distinguishes mono- and bi-layer regions while revealing defect motifs that limit yield and lifetime.[55,56] Top-down thinning/dealloying is exemplified by free-standing monatomic Au and by theory-led alloy screening concepts that exploit selective sputtering windows to bias reconstruction toward monoatomic remnants.[34,37,38,52,53] In both cases, the practical lever is not simply total dose but dose delivery strategy (where and how the beam is scanned), because it determines whether the system reconstructs *via* diffusion and edge capture or instead undergoes net atom loss and catastrophic perforation.[37,38,54] This is where automation, machine learning (ML), and artificial intelligence (AI) become enabling rather than cosmetic: automation provides software-controlled beam delivery and data acquisition; ML provides models trained on microscopy data to detect and quantify features such as thickness, defects, and edge states; and AI provides decision/optimization layers that select actions (often using ML outputs) to achieve a target outcome under constraints. The broader microscopy community is already moving toward data-driven TEM/STEM workflows that treat the instrument as a controllable experimental platform rather than a passive imaging tool.[63] For beam-enabled 2D metals/oxides, a natural next step is closed-loop fabrication, in which the microscope streams images/spectra, analysis models infer thickness/defects/edge configuration, and a control layer updates scan paths and dwell patterns to maximize a chosen objective (*e.g.*, monoatomic area, ribbon continuity, or defect density) while respecting damage limits.[37,38,54,56,64] Early demonstrations of automated/closed-loop STEM control guided by sparse data analytics indicate that on-the-fly decision-making is technically realistic and can reduce reliance on *post hoc* best-frame curation.[64] Deep-learning approaches that identify atomic-scale motifs and subtle distortions provide the analysis backbone for such feedback control.[65]

A second practical opportunity is automated structure discovery and standardized labelling at the atomistic level. Near-term tools that robustly segment monolayer *vs.* multilayer regions, quantify thickness populations, and extract defect and edge statistics would remove a major bottleneck: these tasks are time-intensive, depend strongly on expert judgment, and currently limit cross-study comparability.[52,53,55] Recent ML-driven approaches for automating structural discovery in microscopy data point toward transferable pipelines that operate across materials families and imaging conditions, accelerating comparison between reports and enabling shared, reusable training datasets.[63,65,66] Once such datasets exist, they can be coupled to theory (density functional theory (DFT)/molecular dynamics (MD), edge-energy descriptions, and selective sputtering models) to learn empirical process maps linking beam parameters and boundary conditions to observed outcomes (membrane *vs.* patch *vs.* ribbon), closing the loop between prediction and experiment.[31–34,37,38]

Finally, the longer-term impact will likely come from applications that exploit the non-equilibrium and interface-stabilized nature of freestanding monoatomic systems rather than treating them as fragile curiosities. Their extreme surface exposure, unconventional coordination environments, and tuneable defect chemistries suggest opportunities in catalysis, sensing, and ion transport, particularly where edges and low coordination dominate function.[26,31,32,35,46,55] In parallel, applied interfaces relevance will increasingly be judged by whether these atomically thin architectures can be integrated into devices with controlled injection and minimal parasitic barriers, *i.e.*, by contact engineering. Across 2D semiconductors, contact resistance, barrier formation, and Fermi-level pinning frequently dominate performance and variability, motivating interface-first strategies such as chemically doped injection regions, metallic-phase contacts, edge contacts, and van der Waals junctions that reduce interfacial disorder.[67–73] These concepts are directly aligned with the present review's emphasis on interface definition and cleanliness: at the atomic limit, interfacial structure is not a boundary condition but a design variable. The field should also anticipate convergence with the broader self-driving laboratory paradigm, namely, autonomous experimental design, adaptive execution, and rapid model updating, applied here to electron-beam nanofabrication where

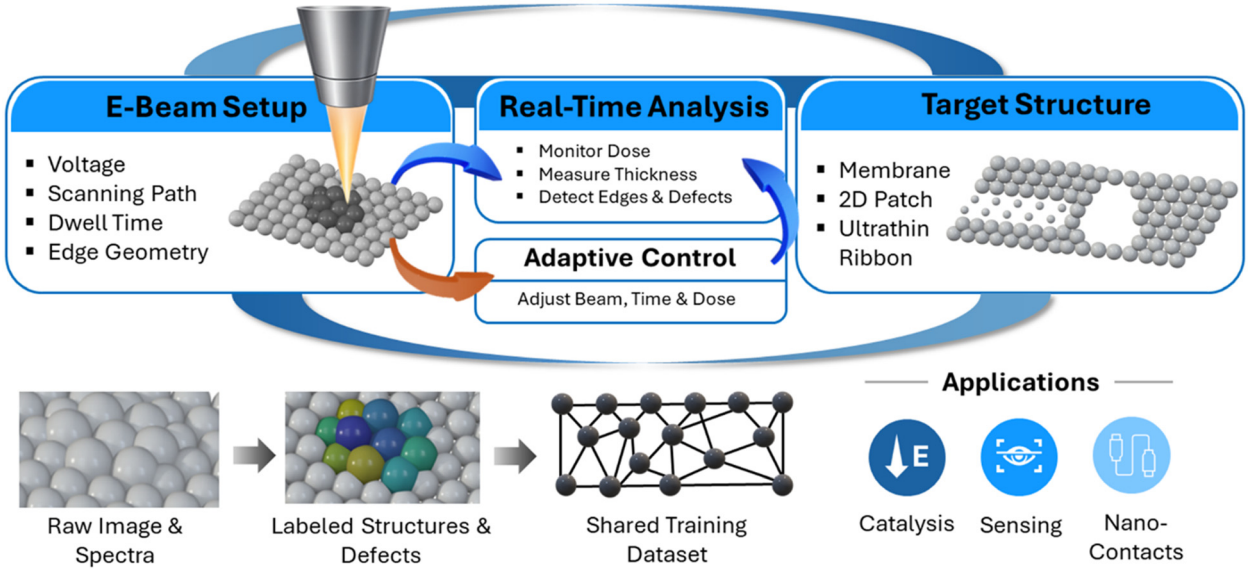

Fig. 9 Conceptual schematic of closed-loop, data-driven electron-beam fabrication of freestanding monoatomic metals and oxides. Electron-beam parameters (voltage, scan path, dwell time, and edge geometry) define an interface-confined reaction space in which real-time analysis quantifies thickness, dose, defects, and edge states. These measurements feed an adaptive control layer that updates beam conditions to steer the system toward target structures, including suspended membranes, finite 2D patches, or ultranarrow ribbons. Automated labelling of atomic-resolution images and spectra enables the creation of shared training datasets, supporting reproducible fabrication and future application-oriented interface architectures.

reactor and metrology are the same instrument.[74] From a materials-ML perspective, beam-enabled monoatomic metals/oxides may become a compact but powerful testbed for active-learning strategies because each experiment yields high-information atomic-structure data, and mechanistic hypotheses (edge stabilization, selective sputtering windows, defect-controlled stability) can be iterated rapidly (Fig. 9).[34,37,38,74–77]

Summary and key conclusions

This review has focused on a deliberately strict definition of freestanding single-atom-thick metals and metal oxides: atomically thin regions suspended without an underlying solid substrate, exposing both faces and supported only at their perimeter (typically by a graphene pore edge). Within this definition, the central theme that emerges across all reported examples is that the electron microscope is simultaneously metrology and reactor: the beam supplies energy/momentum that enables atomic transport, selective atom loss, and reconstruction, while the supporting edge/interface provides the boundary condition that stabilizes otherwise non-layered metallic and oxide lattices at the monatomic limit. The feasibility of these freestanding structures therefore depends less on exfoliation-like logic and more on a coupled electron-beam–interface–finite-size phase space. Across the literature, three experimentally grounded formation routes dominate.

(I) Graphene-pore templating provides the cleanest realization of the freestanding geometry: pore edges localize adatoms/clusters, stabilize low-coordination, quasi-2D atomic configurations *via* edge bonding and geometric confinement, and mechanically anchor membranes, ribbons, and finite planar patches. In this category, the canonical milestones are pore-spanning Fe (and later Cr) membranes, where atomic-resolution imaging plus reciprocal-space analysis and quantitative image/intensity comparisons establish single-atom thickness and crystallinity. The same confinement logic extends to freestanding oxides inside pores (*e.g.*, reconstructed ZnO and CuO), showing that pore stabilization can support non–van der Waals oxide polymorphs, including lattices beyond honeycomb motifs. Importantly, many 2D metal outcomes in pores are not macroscopic sheets but finite, countable patches (*e.g.*, Pt, Sn), consistent with theory emphasizing edge/vacancy energetics and liquid-drop-style scaling in pores.

(II) Subtractive beam chemistry expands the accessible library by treating the beam as a selective chemical driver: a suspended compound precursor is converted into a new 2D phase through preferential sputtering/desorption of a sublattice (*e.g.*, halogens or chalcogens), followed by rapid lattice relaxation into an atomically thin product that is stabilized by confinement and edges. In Fig. 8(a–d), layered metal oxyhalides convert to freestanding single-layer oxides, demonstrating that conversion can yield structurally defined monolayers rather than amorphous remnants. In Fig. 8(e–k), the $MoSe_2$ → Mo membrane transformation provides a clear example where electron beam driven damage becomes a fabrication pathway: atomic-resolution ADF-STEM distinguishes mono- and bi-layer regions and reveals the defect motifs that ultimately delimit membrane yield and

lifetime, with radiation-damage physics being inseparable from synthesis in such beam-enabled routes.

(III) Top-down thinning and alloy-enabled routes leverage thickness self-limitation and selective removal from thicker precursors (including alloys), with reconstruction governed by irradiation history, surface diffusion, and boundary stabilization. The free-standing monatomic Au work is especially valuable because it pairs a substrate-free claim with a rigorous thickness-verification workflow (quantitative ADF-STEM contrast, thickness-population separation, and atom-counting logic). Complementary theory on alloy pairs formalizes a practical screening principle: successful dealloying-to-monolayer outcomes require a meaningful selectivity window so that one component can be removed before the remaining species is destabilized.

A cross-cutting outcome is that, under continued irradiation in confined geometries, the system frequently evolves toward ultranarrow nanoribbons rather than remaining as compact patches or filling pores as extended membranes. This observation aligns with the finite-size/interface perspective: when edge energetics and edge anchoring dominate over bulk-like 2D cohesion, high-aspect-ratio motifs (ribbons/filaments) can become the kinetically selected, longest-lived endpoint under a given dose-rate/voltage window.

Finally, a broader evidentiary lesson, relevant across 2D materials and especially for beam-engineered 2D oxides and non–van der Waals monolayers, is that stability, transformation, and damage are inseparable at the atomic limit: the beam both reveals and reshapes structure, while interfaces and edges set the boundary conditions for what phases can persist. The most convincing studies therefore pair time-resolved (*in situ*) sequences with quantitative thickness/stoichiometry verification (ADF-STEM contrast statistics, image simulations or atom-counting where appropriate, and uncertainty-aware interpretation), and they report the full irradiation recipe (dose, dose rate, scan strategy/probe conditions, environment/cleanliness, and history), not merely the accelerating voltage. This is particularly important for ultrathin ribbons, patch-to-ribbon evolution, and edge-thickened regions, where projection effects and boundary artefacts can masquerade as monolayer contrast unless validated quantitatively and dynamically. Looking ahead, these beam–interface nanoreactor concepts point to a future where atomically thin metals and oxides are not only observed but reliably manufactured: programmable e-beam patterning, combined with automated metrology and closed-loop control, should enable on-demand writing/erasing of monolayer patches and ultranarrow ribbons with targeted composition and defect content. In parallel, integration with data-driven modelling and *in situ* analytics will accelerate discovery of new metastable 2D polymorphs and unlock device-relevant architectures (contacts, interconnects, selective membranes, and catalytic motifs) that are inaccessible by conventional growth routes.

Conflicts of interest

There are no conflicts to declare.

Data availability

No new experimental or computational data were generated as part of this review. Raw versions of selected figures, prior to reproduction or reformatting, have been deposited on Zenodo to support transparency and traceability of the reviewed literature and are available at: https://doi.org/10.5281/zenodo.18219272.

Acknowledgements

A. B., M. Z., S. A. & M. H. R. are grateful to the European Union's Horizon Europe research and innovation program under grant agreement No. 101087143 (Electron Beam Emergent Additive Manufacturing (EBEAM)). A. B. thanks the National Science Center, project 2021/41/B/ST5/04328 X. Y. thanks the Jiangsu Provincial Major Science and Technology Program (Grant No. G2025034) MHR is grateful to National Natural Science Foundation of China (Grant No. 52071225).

References

1 K. S. Novoselov, A. K. Geim, S. V. Morozov, D. Jiang, M. I. Katsnelson, I. V. Grigorieva, S. V. Dubonos and A. A. Firsov, *Nature*, 2005, **438**, 197.
2 Y. B. Zhang, Y. W. Tan, H. L. Stormer and P. Kim, *Nature*, 2005, **438**, 201.
3 K. S. Novoselov, A. K. Geim, S. V. Morozov, D. Jiang, Y. Zhang, S. V. Dubonos, I. V. Grigorieva and A. A. Firsov, *Science*, 2004, **306**, 666.
4 X. Wang, Y. Ouyang, X. Li, H. Wang, J. Guo and H. Dai, *Phys. Rev. Lett.*, 2008, **100**, 206803.
5 A. A. Balandin, *Nat. Mater.*, 2011, **10**, 569.
6 F. Yin, J. Akola, P. Koskinen, M. Manninen and R. E. Palmer, *Phys. Rev. Lett.*, 2009, **102**, 106102.
7 F. Yin, P. Koskinen, S. Kulju, J. Akola and R. E. Palmer, *Sci. Rep.*, 2015, **5**, 8276.
8 F. Yin, S. Kulju, P. Koskinen, J. Akola and R. E. Palmer, *Sci. Rep.*, 2015, **5**, 10065.
9 T. Zhang, P. Cheng, W.-J. Li, Y.-J. Sun, G. Wang, X.-G. Zhu, K. He, L. Wang, X. Ma, X. Chen, Y. Wang, Y. Liu, H.-Q. Lin, J.-F. Jia and Q.-K. Xue, *Nat. Phys.*, 2010, **6**, 104.
10 L. Li, Y. Wang, S. Xie, X.-B. Li, Y.-Q. Wang, R. Wu, H. Sun, S. Zhang and H.-J. Gao, *Nano Lett.*, 2013, **13**, 4671.
11 H. Duan, N. Yan, R. Yu, C.-R. Chang, G. Zhou, H.-S. Hu, H. Rong, Z. Niu, J. Mao, H. Asakura, T. Tanaka, P. J. Dyson, J. Li and Y. Li, *Nat. Commun.*, 2014, **5**, 3093.
12 V. Kochat, A. Samanta, Y. Zhang, S. Bhowmick, P. Manimunda, S. A. S. Asif, A. Stender, R. Vajtai, A. K. Singh, C. S. Tiwary and P. M. Ajayan, *Sci. Adv.*, 2018, **4**, e1701373.
13 V. Kochat, *et al.*, *Sci. Adv.*, 2018, **4**, e1701373.
14 M. Houssa, A. Dimoulas and A. Molle, *J. Phys.: Condens. Matter*, 2015, **27**, 253002.

15 F.-f. Zhu, W.-j. Chen, Y. Xu, C.-l. Gao, D.-d. Guan, C.-h. Liu, D. Qian, S.-C. Zhang and J.-f. Jia, *Nat. Mater.*, 2015, **14**, 1020.
16 J. Deng, B. Xia, X. Ma, H. Chen, H. Shan, X. Zhai, B. Li, A. Zhao, Y. Xu, W. Duan, S.-C. Zhang, B. Wang and J. G. Hou, *Nat. Mater.*, 2018, **17**, 1081.
17 J. Yuhara, H. Shimazu, K. Ito, A. Ohta, M. Araidai, M. Kurosawa, M. Nakatake and G. Le Lay, *ACS Nano*, 2018, **12**, 11632.
18 M. Fortin-Deschenes, O. Waller, T. O. Menteş, A. Locatelli, S. Mukherjee, F. Genuzio, P. L. Levesque, A. Heibert, R. Martel and O. Moutanabbir, *Nano Lett.*, 2017, **17**, 4970.
19 J. Yuhara, B. He, N. Matsunami, M. Nakatake and G. Le Lay, *Adv. Mater.*, 2019, **31**, 1901017.
20 T. Zhang, *et al.*, *Nat. Phys.*, 2010, **6**, 104.
21 S. Xiao, *et al.*, *Nano Res.*, 2022, **15**, 3770.
22 P. Rosenzweig and U. Starke, *Phys. Rev. B*, 2020, **101**, 201407(R).
23 Y. Su, E. Prestat, C. Hu, V. K. Puthiyapura, M. Neek-Amal, H. Xiao, K. Huang, V. G. Kravets, S. J. Haigh, C. Hardacre, F. M. Peeters and R. R. Nair, *Nano Lett.*, 2019, **19**, 4678–4683.
24 A. V. Krasheninnikov, Y.-C. Lin and K. Suenaga, *Nano Lett.*, 2024, **24**, 12733–12740.
25 H. Duan, *et al.*, *Nat. Commun.*, 2014, **5**, 3093.
26 J. Zhao, Q. Deng, A. Bachmatiuk, G. Sandeep, A. Popov, J. Eckert and M. H. Rümmeli, *Science*, 2014, **343**, 1228.
27 L.-M. Yang, M. Dornfeld, T. Frauenheim and E. Ganz, *Phys. Chem. Chem. Phys.*, 2015, **17**, 26036.
28 L.-M. Yang, T. Frauenheim and E. Ganz, *Phys. Chem. Chem. Phys.*, 2015, **17**, 19695.
29 L.-M. Yang, T. Frauenheim and E. Ganz, *J. Nanomater.*, 2016, **2016**, 8429510.
30 J. Nevalaita and P. Koskinen, *Phys. Rev. B*, 2018, **97**, 035411.
31 J. Nevalaita and P. Koskinen, *Phys. Rev. B*, 2018, **98**, 115433.
32 J. Nevalaita and P. Koskinen, *Nanoscale*, 2019, **11**, 22019–22024.
33 S. Ono and P. Koskinen, *Phys. Rev. B*, 2020, **102**, 165424.
34 J. Nevalaita and P. Koskinen, *AIP Adv.*, 2020, **10**, 065327.
35 H. Quang, A. Bachmatiuk, A. Dianat, F. Ortmann, J. Zhao, J. Warner, J. Eckert, G. Cunniberti and M. Rümmeli, *ACS Nano*, 2015, **9**, 11408.
36 W. Zhou, M. Gao and D. Guo, *et al.*, *Res. Sq.*, 2025, DOI: 10.21203/rs.3.rs-7893525/v1.
37 R. F. Egerton, P. Li and M. Malac, *Micron*, 2004, **35**, 399–409.
38 A. V. Krasheninnikov and K. Nordlund, *J. Appl. Phys.*, 2010, **107**, 071301.
39 H. Q. Ta, Q. X. Yang, S. Liu, A. Bachmatiuk, R. G. Mendes, T. Gemming and Y. Liu, *et al.*, *Nano Lett.*, 2020, **20**, 4354–4361.
40 Y. Shao, R. Pang and X. Shi, *J. Phys. Chem. C*, 2015, **119**, 22954–22960.
41 R. G. Mendes, *et al.*, *Adv. Funct. Mater.*, 2025, **35**, 2412889.
42 L. Zhao, *et al.*, *Adv. Mater. Interfaces*, 2020, **7**, 2000436.
43 S. Antikainen and P. Koskinen, *Comput. Mater. Sci.*, 2017, **131**, 120–125.
44 P. Koskinen and T. Korhonen, *Nanoscale*, 2015, **7**, 10140–10145.
45 K. Yin, Y.-Y. Zhang, Y. Zhou, L. Sun, M. F. Chisholm, S. T. Pantelides and W. Zhou, *2D Mater.*, 2017, **4**, 011001.
46 H. Q. Ta, *et al.*, *Crystals*, 2016, **8**, 100.
47 C. Z. Dong, W. P. Zhu, S. Y. Zhao, P. Wang, H. T. Wang and W. Yang, *J. Appl. Mech.*, 2013, **80**, 040904.
48 X. Yang, H. Q. Ta, W. Li, R. G. Mendes, Y. Liu, Q. Shi, S. Ullah, A. Bachmatiuk, J. Luo, L. Liu, J.-H. Choi and M. H. Rümmeli, *Nano Res.*, 2021, **14**, 747–753.
49 J. A. Rodríguez-Manzo, O. Cretu and F. Banhart, *ACS Nano*, 2010, **4**, 3422–3428.
50 A. W. Robertson, B. Montanari, K. He, J. Kim, C. S. Allen, Y. A. Wu, J. Olivier, J. Neethling, N. Harrison, A. I. Kirkland and J. H. Warner, *Nano Lett.*, 2013, **13**, 1468–1475.
51 R. G. Mendes, H. Q. Ta, X. Yang, W. Li, A. Bachmatiuk and J.-H. Choi, *et al.*, *Small*, 2020, **16**, 1907115.
52 X. Wang, *et al.*, *Nano Lett.*, 2019, **19**, 4560–4566.
53 J. M. LeBeau, S. D. Findlay, L. J. Allen and S. Stemmer, *Nano Lett.*, 2010, **10**, 4405–4408.
54 X. Zhao, J. Kotakoski, J. C. Meyer, E. Sutter, P. Sutter, A. V. Krasheninnikov, U. Kaiser and W. Zhou, *MRS Bull.*, 2017, **42**, 667–676.
55 X. Zhao, J. Dan, J. Chen, Z. Ding, W. Zhou, K. P. Loh and S. J. Pennycook, *Adv. Mater.*, 2018, **30**, 1707281.
56 T. Lehnert, O. Lehtinen, G. Algara-Siller and U. Kaiser, *Appl. Phys. Lett.*, 2017, **110**, 033106.
57 R. F. Egerton, *Ultramicroscopy*, 2013, **127**, 100–108.
58 N. Jiang, *Rep. Prog. Phys.*, 2016, **79**, 016501.
59 F. Banhart, J. Kotakoski and A. V. Krasheninnikov, *ACS Nano*, 2011, **5**, 26–41.
60 O. Lehtinen, S. Kurasch, A. V. Krasheninnikov and U. Kaiser, *Nat. Commun.*, 2013, **4**, 2098.
61 J. C. Meyer, S. Kurasch, H. J. Park, V. Skakalova, D. Künzel, A. Gross, A. Chuvilin, G. Algara-Siller, S. Roth, T. Iwasaki, U. Starke, J. H. Smet and U. Kaiser, *Nat. Mater.*, 2011, **10**, 209–215.
62 F. Banhart, *Rep. Prog. Phys.*, 1999, **62**, 1181–1221.
63 S. R. Spurgeon, C. Ophus, L. Jones, A. Petford-Long, S. V. Kalinin, M. J. Olszta, R. E. Dunin-Borkowski, N. Salmon, K. Hattar and W.-c. D. Yang, *Nat. Mater.*, 2021, **20**, 274–279.
64 M. Olszta, D. Hopkins, K. R. Fiedler, M. Oostrom, S. Akers and S. R. Spurgeon, *Microsc. Microanal.*, 2022, **28**, 1611–1621.
65 M. Ziatdinov, O. Dyck, A. Maksov, B. M. Hudak, A. R. Lupini, J. Song, P. C. Snijders, R. K. Vasudevan, S. Jesse and S. V. Kalinin, 2018, arXiv:1801.05133, DOI: 10.48550/arXiv.1801.05133.
66 N. C. Creange, O. Dyck, R. K. Vasudevan, M. Ziatdinov and S. V. Kalinin, *Mach. Learn.: Sci. Technol.*, 2022, **3**, 015024.
67 J. P. Allain, J. Kang, K. Banerjee and A. Kis, *Nat. Mater.*, 2015, **14**, 1195–1205.
68 H. Fang, S. Chuang, T. C. Chang, K. Takei, T. Takahashi and A. Javey, *Nano Lett.*, 2012, **12**, 3788–3792.
69 R. Kappera, D. Voiry, S. E. Yalcin, B. Branch, G. Gupta, A. D. Mohite and M. Chhowalla, *Nat. Mater.*, 2014, **13**, 1128–1134.
70 L. Wang, I. Meric, P. Y. Huang, Q. Gao, Y. Gao, H. Tran, T. Taniguchi, K. Watanabe, L. M. Campos, D. A. Muller, J. Guo,

P. Kim, J. Hone, K. L. Shepard and C. R. Dean, *Science*, 2013, **342**, 614–617.
71 Y. Liu, N. O. Weiss, X. Duan, H. C. Cheng, Y. Huang and X. Duan, *Nat. Rev. Mater.*, 2016, **1**, 16042.
72 S. Das, H. Y. Chen, A. V. Penumatcha and J. Appenzeller, *Nano Lett.*, 2013, **13**, 100–105.
73 Y. Liu, P. Stradins and S.-H. Wei, *Sci. Adv.*, 2016, **2**, e1600069.
74 M. Seifrid, R. Pollice, A. Aguilar-Granda, Z. M. Chan, K. Hotta, C. T. Ser, J. Vestfrid, T. C. Wu and A. Aspuru-Guzik, *Acc. Chem. Res.*, 2022, **55**, 2454–2466.
75 C. Ophus, *Microsc. Microanal.*, 2019, **25**, 563–582.
76 K. T. Butler, D. W. Davies, H. Cartwright, O. Isayev and A. Walsh, *Nature*, 2018, **559**, 547–555.
77 L. M. Roch, F. Häse, C. Kreisbeck, T. Tamayo-Mendoza, L. P. E. Yunker, J. E. Hein and A. Aspuru-Guzik, *PLoS One*, 2020, **15**, e0229862.